Interlayer Exchange Coupling in Magnetic Hard-Soft Bilayered Structures

Daniel Richardson,[1] Kumar Srinivasan,[2] Alan Kalitsov,[2] Antony Ajan,[2] Shikha Jain,[2] Sidney Katz,[1] and Mingzhong Wu[1,*]

[1] *Department of Physics, Colorado State University, Fort Collins, Colorado 80523, USA*
[2] *Western Digital, San Jose, California 95131, USA*

(Received 28 November 2018; revised manuscript received 18 February 2019; published 5 April 2019)

Broadband ferromagnetic resonance (FMR) and high-temperature (T) FMR measurements are carried out to study interlayer exchange coupling (IEC) in a magnetic hard-soft bilayered system where the hard layer is a FePt thin film with strong perpendicular anisotropy and the soft layer is a thin film made of Fe, Co, or their alloys. The data indicate that the effective exchange field (H_{ex}) produced by the IEC on the soft layer increases with a decrease in the thickness or saturation induction ($4\pi M_s$) of the soft layer. With an increase in T, H_{ex} drops by an amount larger than $4\pi M_s$. The effective damping constant of the soft layer increases with H_{ex} and can vary by two orders of magnitude. In samples with $H_{\mathrm{ex}} > 4\pi M_s$, the damping constant is insensitive to the choice of material of the soft layer. In samples with $H_{\mathrm{ex}} < 4\pi M_s$, the damping constant strongly depends on the choice of material. When T is increased from room temperature to the Curie temperature of the hard layer, the FMR linewidth drops significantly in samples where H_{ex} is relatively large, but remains constant or even increases slightly at high T in samples where H_{ex} is very small. The effects of H_{ex} on the damping and linewidth can be understood by considering two distinct components in the overall damping, an intrinsic component mainly due to spin-flip magnon-electron scattering and an extrinsic component due to IEC-associated spin pumping at the interface.

DOI: 10.1103/PhysRevApplied.11.044016

I. INTRODUCTION

Bilayered systems that consist of a hard magnetic layer and a soft magnetic layer are of great interest. On one hand, it is fundamentally interesting to understand how the magnetic properties of one layer are influenced by the other layer via direct exchange coupling at the interface. On the other hand, the fact that the soft layer can significantly ease the magnetization reversal in the hard layer through a so-called exchange spring mechanism [1,2] makes the hard-soft bilayered structure a very attractive material system for energy-efficient, high-density data storage applications [3,4].

Despite the fundamental and technological importance of the hard-soft bilayered system, systematic experimental studies on how to control the interlayer exchange coupling (IEC) and how the IEC affects the dynamics in each layer are limited. This article reports on the IEC in a bilayered structure where the hard layer is a $L1_0$-ordered FePt thin film with strong perpendicular magnetic anisotropy (PMA) and the soft layer is a thin film made of ferromagnetic transition metals (FTM) Fe, Co, or their alloys. Comprehensive ferromagnetic resonance (FMR) studies are carried out on this bilayered system to explore (1) how the IEC-produced effective exchange field (H_{ex}) on the soft layer varies with the soft layer thickness, the material choice of the soft layer, and the temperature and (2) how H_{ex} affects the FMR linewidth and damping of the soft layer.

The key results are as follows. First, the effective exchange field (H_{ex}) on the soft layer increases with a decrease in the soft layer thickness (d). There exists a critical thickness below which one has $H_{\mathrm{ex}} > 4\pi M_s$ and above which one has $H_{\mathrm{ex}} < 4\pi M_s$, where M_s denotes the saturation magnetization of the soft layer and $4\pi M_s$ is the saturation induction. The critical thickness for this transition depends on the material of the soft layer and generally increases with a decrease in $4\pi M_s$. These results are consistent with the general expectation of $H_{\mathrm{ex}} \propto (M_s \cdot d)^{-1}$. Second, when the temperature (T) is increased toward the Curie temperature (T_c) of the hard layer, H_{ex} drops by an amount larger than $4\pi M_s$, mainly because T_c of the hard layer is lower than that of the soft layer. Third, the damping of the soft layer increases with H_{ex}. By varying H_{ex}, the effective Gilbert damping constant (α_{eff}) can be tuned over two orders of magnitude, from 0.0055 to 0.552. Fourth, the damping of the soft layer is relatively insensitive to the choice of the material in the "$H_{\mathrm{ex}} > 4\pi M_s$" regime, but strongly depends on the material in the "$H_{\mathrm{ex}} < 4\pi M_s$" regime. Finally, with an increase in T, the FMR linewidth of the soft layer decreases substantially in structures with relatively large H_{ex}, but remains constant in structures with very small H_{ex}. The last three results can be understood in

*mwu@colostate.edu

terms of the relative contributions of the intrinsic damping and the spin pumping to the overall damping. Here, spin pumping refers to the process in which the magnetization precession in the soft layer pumps a spin current to the hard layer, in a manner similar to the spin pumping effect in ferromagnet-normal metal heterostructures [5–8].

Four important points should be mentioned. (1) The hard-soft FePt/FTM system studied in this work is of great technological interest [9–12]. This is because this system has been widely accepted as the media material for next-generation heat-assisted magnetic recording (HAMR) drives [13]. (2) The conclusions from this work are of a general nature and can be applied to many other hard-soft bilayered systems, although they are drawn from a particular FePt/FTM system. (3) Although this study does not address how the IEC varies with the properties of and affects the damping in the hard layer, this question is equally important and is worthy of being explored in the future. (4) The discussions below focus on the effective exchange field H_{ex}, which is produced by IEC. Future studies that characterize and measure IEC in bilayered systems using other parameters, such as an exchange length and an effective exchange constant, are of great interest.

II. MEASUREMENT SAMPLES

This study uses of twenty FePt/FTM samples, which are prepared by dc sputtering under the exact same conditions. The hard layers, grown on glass substrates, are the same in all twenty samples. They are 10-nm thick $L1_0$-ordered FePt granular films with the segregants at the grain boundaries made of C and SiO_2. However, the soft layers, which are grown directly on top of the hard layers, are all different. They are either made of different materials or are made of the same material but with different thicknesses. Table I lists the main properties of the soft FTM layers; the thicknesses are nominal values estimated on the basis of the sputtering growth rate, and the $4\pi M_s$ values are all literature values [14]. To protect the soft FTM layers from oxidation, all samples are capped with a 3-nm thick carbon layer. The samples for the FMR measurements are all circular, with a diameter of about 2 mm.

The structural properties of the samples are characterized by XRD, TEM, and EELS techniques. The XRD and TEM data confirm the $L1_0$ phase of the FePt films, as discussed in Ref. [15]. Note that the FePt films in the samples studied here show structural properties very similar to those of sample $S8$ in Ref. [15]. Figure 1 shows representative cross-section TEM images obtained on the FePt/Co bilayered samples. The images clearly show the granular nature of the hard FePt layer and the continuous, nongranular nature of the soft Co layer. One can also see that the FePt/Co interfaces are not smooth, which makes the use of TEM analyses to accurately determine the thickness values of the soft Co layers impossible. This is why Table I lists the nominal thickness values. It is for the same reason that Table I gives the literature $4\pi M_s$ values; the determination of the actual $4\pi M_s$ values needs to take into account the film thickness and thus carries forward the errors in the film thickness estimation.

TABLE I. Properties of the FTM layers in hard-soft FePt/FTM bilayered samples.

Material	Thickness (nm)	$4\pi M_s$ (kG)
Fe	2.7, 3.3, 4.0, 4.7	20.7
$Fe_{60}Co_{40}$	3.2, 4.3, 5.8	23.8
$Fe_{40}Co_{60}$	2.9, 4.3, 5.8, 7.2	23.0
$Fe_{10}Co_{90}$	3.2, 4.3, 5.8	19.2
Co	3.2, 4.3, 5.8	17.7
$Co_{95}Nd_5$	4.3, 5.8, 7.2	-

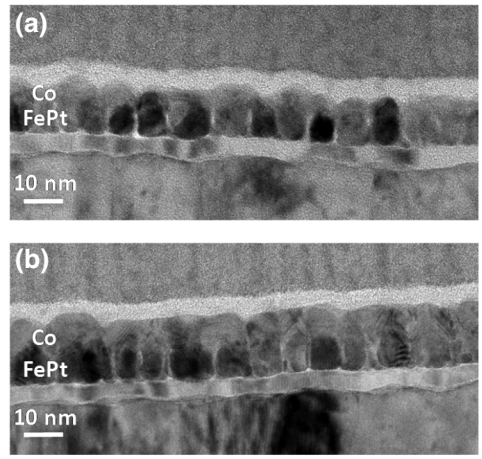

FIG. 1. Cross-section TEM images of FePt/Co bilayered samples. (a) Image of a FePt/Co(3.2 nm) sample. (b) Image of a FePt/Co(5.8 nm) sample.

The static magnetic properties of the samples are measured by polar magneto-optical Kerr effect (MOKE) techniques; the detailed data are presented in the Appendix section. The magnetic hysteresis loops all look clean and smooth and show almost 100% remanence at zero fields. No two-stage switching is observed. These results show that the hard FePt layers have perpendicular anisotropy and the soft FTM layers are tightly coupled to the FePt layers. The MOKE data also show that for a given soft material, the coercivity of the bilayered sample decreases with an increase in the thickness of the soft layer and for a given soft layer thickness, the coercivity varies with the choice of the soft material. These results are consistent with the general expectation on the roles of the soft layer in the switching of the hard layer in a hard-soft bilayered system.

III. BROADBAND FMR APPROACH

The FMR measurements include (1) frequency-dependent FMR measurements using a coplanar waveguide (CPW)

and a vector network analyzer (VNA) at room temperature [16,17] and (2) temperature-dependent FMR measurements using a microwave cavity [18]. Figure 2 shows the experimental configuration and representative data for frequency-dependent FMR measurements. Figure 2(a) sketches the experimental setup, which mainly consists of a CPW device and a VNA. The CPW has a 50-μm wide signal line, a signal line-to-ground spacing of 25 μm, and a nominal impedance of 50 Ω. The sample is placed on the CPW with the soft layer side facing the CPW structure and the substrate side facing up. An external static magnetic field (H) is applied perpendicular to the sample plane to either magnetize the sample to saturation or enable FMR measurements. The measurement and data analysis procedures involve the following major steps:

(1) Magnetize the sample with a large magnetic field. For the data shown below, this field is 80 kOe.

(2) Measure the complex transmission coefficient S_{21} of the CPW/sample structure as a function of H at a fixed microwave frequency (f). Note that the field in this process is significantly smaller than that in (1). Figure 2(b) presents representative S_{21} data, which are obtained at $f = 29$ GHz with a sample where the soft layer is made of a 4.3-nm thick $Co_{60}Fe_{40}$ film. The data show a clear resonance response, which corresponds to the FMR of the soft layer. The FMR of the hard layer is at a significantly higher frequency at room temperature due to the strong PMA field in the hard layer [19].

(3) Numerically fit the real and imaginary parts of S_{21} with theoretical S_{21} profiles [20,21] to determine the FMR field (H_{FMR}) and the FMR linewidth (ΔH). The red curves in Fig. 2(b) show such numerical fits.

(4) Repeat steps (1)–(3) for different microwave frequencies.

(5) Plot H_{FMR} vs f and then fit the data, as shown in Fig. 2(c), using

$$f = |\gamma|(H_{\mathrm{FMR}} + H_{\mathrm{eff}}), \tag{1}$$

where $|\gamma|$ is the absolute gyromagnetic ratio and H_{eff} is the effective internal field and can be written as

$$H_{\mathrm{eff}} = H_{\mathrm{ex}} - 4\pi M_s, \tag{2}$$

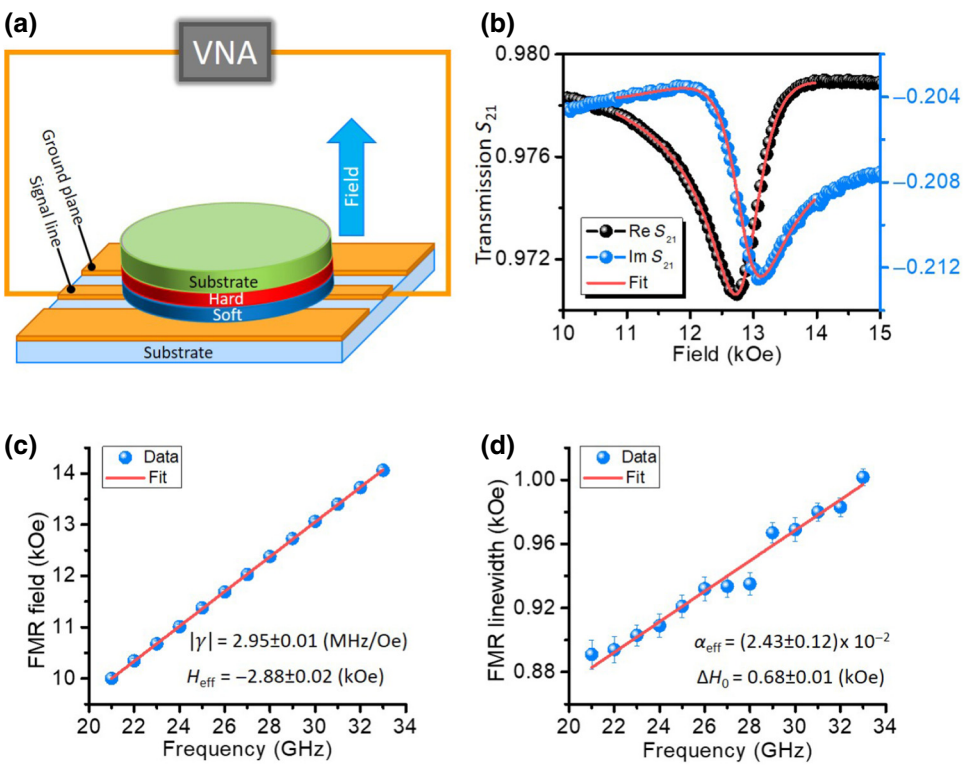

FIG. 2. Broadband FMR measurements. (a) Experimental configuration. (b)-(d) Representative data measured on a FePt/$Co_{60}Fe_{40}$(4.3 nm) bilayered sample. (b) The real and imaginary parts of the complex transmission coefficient S_{21} of the CPW/sample structure measured as a function of the magnetic field at a microwave frequency (f) of 29 GHz. The dots show the data, while the red curves show numerical fits to theoretical S_{21} profiles. (c) FMR field vs f. The blue dots present the data, while the red line is a numerical fit to Eq. (1). The fitting yields the absolute gyromagnetic ratio $|\gamma|$ and the effective internal field H_{eff} as indicated. (d) FMR linewidth vs f. The blue dots present the data, while the red line is a fit to Eq. (3). The fitting yields the effective Gilbert damping constant α_{eff} and the inhomogeneity line broadening contribution ΔH_0 as indicated.

where $4\pi M_s$ is the saturation induction of the soft layer. Note that both $|\gamma|$ and H_{eff} are the fitting parameters and for the fit shown in Fig. 2(c), the corresponding values are indicated in the figure.

(6) Plot ΔH vs f and then fit the data, as shown in Fig. 2(d), using

$$\Delta H = \frac{2\alpha_{\text{eff}}}{|\gamma|} f + \Delta H_0, \tag{3}$$

where ΔH_0 is not associated with the damping but denotes the spatial sample inhomogeneity caused line broadening. α_{eff} and ΔH_0 are the fitting parameters. The corresponding values for the fit in Fig. 2(d) are indicated in the figure. Note that α_{eff} describes the effective damping of the soft layer rather than the overall damping of the entire bilayered system, because the measured resonance is from the FMR in the soft layer, as mentioned above.

IV. RESULTS FROM BROADBAND FMR MEASUREMENTS

Figure 3 presents the data obtained through the above-described procedure. Figure 3(a) gives the effective internal field (H_{eff}) vs soft layer thickness (d) data. The data show a clear trend, H_{eff} increases with a decrease in d. If one considers Eq. (2) and the fact that $4\pi M_s$ is usually independent of d, it can be concluded that H_{ex} is higher in samples with thinner soft layers. Note that although $4\pi M_s$ is an intrinsic property of a magnetic material, it may be possible that in ultrathin films $4\pi M_s$ decreases slightly with a decrease in d due to interfacial diffusion or surface oxidation. However, such a change in $4\pi M_s$, if any, should be relatively small, and it alone cannot account for the large H_{eff} variations shown in Fig. 3(a).

The data in Fig. 3(a) show four important results. (1) H_{ex} increases with a decrease in d, as mentioned above. (2) There exists a critical thickness (d_c). If $d > d_c$, H_{eff} is negative and one has $H_{\text{ex}} < 4\pi M_s$. If $d < d_c$, H_{eff} is positive and one has $H_{\text{ex}} > 4\pi M_s$. (3) d_c strongly depends on the choice of material of the soft layer; except for the samples with the Fe soft layers, the d_c value generally increases with a decrease in $4\pi M_s$. (4) For a given soft layer thickness, the Fe samples show H_{ex} significantly larger than that of other samples. Note that the "$H_{\text{ex}} > 4\pi M_s$" regime corresponds to the situation in which H_{ex} overcomes the demagnetization field in the soft FTM layer, leading to perpendicular orientation of the FTM magnetization in the absence of an external field. In contrast, in the "$H_{\text{ex}} < 4\pi M_s$" regime, the dipolar interactions in the soft FTM layer dominate over H_{ex}, giving rise to in-plane orientation of the FTM magnetization in the absence of an external field.

The first three results discussed above are consistent with the general expectation of $H_{\text{ex}} \propto (M_s \cdot d)^{-1}$ in hard-soft bilayered systems [22]. The reason for the last result is currently unknown. One possible reason is that the first atomic layer of the Fe film near the interface may also serve as the top atomic layer of the FePt film, resulting in a rather strong IEC and large H_{ex}. Those results together clearly suggest that one can tune H_{ex} in hard-soft bilayered systems by either varying the soft layer thickness or using different materials for the soft layer.

Figure 3(b) presents the α_{eff} vs d data. Two results are evident from the data. First, via varying the material and thickness of the soft layer, α_{eff} can be tuned over two orders of magnitude, with the lowest value being 0.0055 and the largest being 0.552. The physical mechanism that enables such a broad tuning range is discussed shortly.

Second, the data show a common trend - α_{eff} increases with a decrease in d. This thickness dependence is relatively weak in the Fe sample, but is very strong in all other samples. For example, in the FePt/$Fe_{40}Co_{60}$ sample, α_{eff} increases by a factor of 43.8 when d is decreased from 5.8 to 2.9 nm. There are two possible reasons for the observed thickness dependence. First, the overall damping in a magnetic thin film may contain a contribution from two-magnon scattering [23–25] associated with surface roughness or defects on the surface or at the interface;

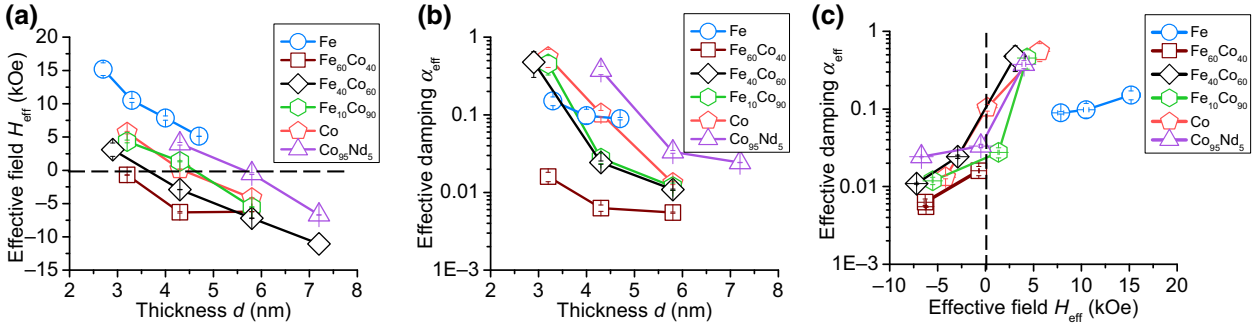

FIG. 3. Data from broadband FMR studies. (a) Effective internal field (H_{eff}) vs soft layer thickness (d) for FePt/FTM bilayered samples where the soft FTM layers are made of different materials as indicated. (b) Effective Gilbert damping constant (α_{eff}) vs d for the same samples as for the data in (a). (c) α_{eff} vs H_{eff}. The H_{eff} data are from (a), while the α_{eff} data are from (b).

the weight of this contribution in the total damping is usually larger in thinner films. However, it seems that this mechanism alone cannot explain the rather big $\alpha_{\rm eff}$ changes shown in Fig. 2(b) if one takes into account that the two-magnon scattering is very weak in films magnetized perpendicularly [26,27]. Second, the observed thickness dependence may be associated mainly with the thickness dependence of $H_{\rm ex}$ since the data in Figs. 3(a) and 3(b) seem to show similar overall trends.

To clarify the above conjecture about the dominant physical mechanism for the strong thickness dependence shown in Fig. 3(b), $\alpha_{\rm eff}$ is plotted against $H_{\rm eff}$ in Fig. 3(c). One can clearly see that $\alpha_{\rm eff}$ increases with $H_{\rm eff}$. This response suggests that $\alpha_{\rm eff}$ increases notably with $H_{\rm ex}$ and the d dependence shown in Fig. 3(b) is associated mainly with the change of $H_{\rm ex}$ with d, not the two-magnon scattering process. In addition, one can also see that the uppermost four data points over the 3–6 kOe field range show similar $\alpha_{\rm eff}$ values, while the left most five points in a relatively narrower field range show very different $\alpha_{\rm eff}$ values, varying by a factor of 5. This result indicates that in the "$H_{\rm ex} > 4\pi M_s$" regime, $\alpha_{\rm eff}$ is insensitive to the choice of the material of the soft layer; in contrast, in the "$H_{\rm ex} < 4\pi M_s$" regime, $\alpha_{\rm eff}$ strongly depends on the choice of the material.

The above results about the damping can be understood by considering the presence of two distinct components in the overall damping constant, namely,

$$\alpha_{\rm eff} = \alpha_0 + \alpha_{\rm sp}, \tag{4}$$

where α_0 denotes the intrinsic damping of the soft layer while $\alpha_{\rm sp}$ describes the extrinsic damping due to the pumping of spin by the precessional motion in the soft layer to the hard layer. As the spin pumping is associated with the exchange coupling of the moments in the soft layer to those in the hard layer, $\alpha_{\rm sp}$ increases with $H_{\rm ex}$. This results in the increasing response shown in Fig. 3(c). As $H_{\rm ex}$ can be tuned over a wide range by varying the choice of the material and the thickness of the soft layer, as shown in Fig. 3(a), $\alpha_{\rm sp}$ can also be changed over a wide range, giving rise to the wide tuning range of the overall damping $\alpha_{\rm eff}$ (two orders of magnitude) shown in Fig. 3(b). In the samples with large $H_{\rm ex}$, $\alpha_{\rm sp}$ can be significantly larger than α_0, which explains the insensitivity of $\alpha_{\rm eff}$ to the choice of the material shown by the uppermost four data points in Fig. 3(c). In contrast, in the samples with relatively low $H_{\rm ex}$, $\alpha_{\rm sp}$ is either comparable to or smaller than α_0, giving rise to the strong dependence of $\alpha_{\rm eff}$ on the choice of the material shown by the left most five data points in Fig. 3(c). Note that α_0 in ferromagnetic FTM thin films results mostly from spin-flip magnon-electron scattering (or interband scattering) and Fermi surface breathing-associated magnon-electron scattering (or intraband scattering), with the former being dominant at high temperatures while the latter is dominant at low temperatures [28–31]. Such scattering strongly depends on the properties of band structures in the material, so α_0 is usually material dependent. Note that magnon-photon scattering and eddy current can also contribute to the overall damping, but their contributions should be much smaller than the damping associated with the magnon-electron scattering in the samples studied in this work.

It should be highlighted that, as shown in Fig. 3(c), the $\alpha_{\rm eff}$ values of the three Fe samples seem to be off the trend. The actual reason for this is currently unknown, but it may share the same origin as the unusual $H_{\rm ex}$ response of the Fe samples discussed above. Two points should be made about the $\alpha_{\rm eff}$ values of the Fe samples. First, they are all substantially larger than the literature α_0 value in Fe, which is about 0.002 [32]. This is likely associated with the presence of the very strong IEC in the Fe samples. Second, they show a $H_{\rm eff}$ dependence much weaker than the $\alpha_{\rm eff}$ values in other samples. This is probably because all three Fe samples are in the "$H_{\rm ex} > 4\pi M_s$" regime, while the other samples exhibit different $H_{\rm ex}$ strengths.

Three notes should be made about the above discussions on the data in Fig. 3. First, the FMR analysis processes described above take a small-damping approximation, namely, $(\alpha_{\rm eff})^2 \ll 1$. In the case where the damping is strong, "$(\alpha_{\rm eff})^2 \ll 1$" is not true anymore and a full numerical analysis of the S_{21} data is needed. The uppermost four data points in Fig. 3(c) are obtained through the full analysis that does not use the small-damping approximation. Details about this analysis are provided in the Appendix section. Second, 20 samples are measured in the experiments, but Fig. 3(b) shows the data for 18 samples only. This is because only a few frequency points are obtained for the 4.7-nm-Fe sample and the 2.9-nm-$Fe_{40}Co_{60}$ sample due to experimental limitation. While the data are enough to reliably determine $H_{\rm eff}$, they do not provide enough information to calculate $\alpha_{\rm eff}$. Third, it is known that $\alpha_{\rm sp}$ depends on the spin mixing conductance at the interface. Thus, it is expected that a change in the material of the soft layer should give rise to a change in the spin mixing conductance and a corresponding variation in $\alpha_{\rm eff}$, but this effect seems to be weak because the data in Fig. 3(c) show that $\alpha_{\rm eff}$ does not notably vary with the choice of the material in the $H_{\rm ex} > 4\pi M_s$ large-$\alpha_{\rm sp}$ regime.

V. HIGH-*T* FMR APPROACH

The data presented above are all measured at room temperature. We now turn to the high-temperature (T) FMR measurements and analyses. Figure 4 shows the high-T FMR approach. Figure 4(a) shows a schematic diagram of the experimental system. The main components include a rectangular microwave cavity (purple), a diamond rod (yellow) with a diameter of 2 mm that loads the sample (red)

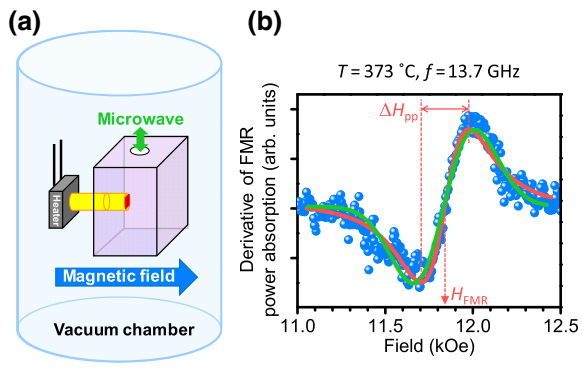

FIG. 4. High-temperature FMR measurements. (a) Schematic diagram of the experimental setup. (b) Representative FMR power absorption data (blue dots), a Lorentzian fit (red curve), and a Gaussian fit (green curve). The data are measured at $T = 373\,°\mathrm{C}$ on a FePt/Co(5.8 nm) bilayered sample. The Lorentzian fit yielded FMR field H_{FMR} and peak-to-peak FMR linewidth ΔH_{pp} are indicated in (b).

into the cavity, and a ceramic heater (gray) that heats the sample through the diamond rod. These components are housed in a high-vacuum chamber and the measurements are performed at a pressure of about 6.7×10^{-3} Pa (or about 5×10^{-5} Torr) to prevent changes in sample properties due to oxygen during high-T measurements as well as to reduce temperature fluctuations during the FMR measurements. For the FMR data presented below, f is kept constant at 13.7 GHz, which is also the resonant frequency of the microwave cavity, while H is swept. Prior to placing the sample in the FMR system, the sample is magnetized by a perpendicular magnetic field of $H = 80$ kOe at room temperature. After placing the sample in the FMR system and heating it, prior to each FMR measurement, the sample is saturated by a field of $H = 15$ kOe. More details about this approach are provided in Ref. [18].

Figure 4(b) presents the FMR data (blue dots) measured at $T = 373\,°\mathrm{C}$ on a sample where the soft layer is made of a 5.8-nm thick Co film. The red curve shows a numerical fit to the derivative of a Lorentzian trial function. The Lorentzian fitting obtained FMR field (H_{FMR}) and peak-to-peak FMR linewidth (ΔH_{pp}) are indicated in the figure. Note that one has $\Delta H_{\mathrm{pp}} = \Delta H/\sqrt{3}$. A fit (green curve) to the derivative of a Gaussian trial function is also included in the figure. One can see that the Lorentzian fit is slightly better than the Gaussian fit, indicating that the inhomogeneity line broadening contribution to ΔH_{pp}, if any, is relatively small. In the case where a film sample has strong spatial inhomogeneity and the associated line broadening (ΔH_0) is large, the Gaussian function would fit the FMR data better than the Lorentzian function [33].

VI. RESULTS FROM HIGH-*T* FMR MEASUREMENTS

The above-described high-T approach is used to study FMR in three samples whose soft layers are made of a 5.8-nm thick $Co_{95}Nd_5$ film, a 7.2-nm thick $Co_{95}Nd_5$ film, and a 5.8-nm thick Co film, respectively. These three samples are chosen because they show moderate α_{eff} at room temperature, as shown in Fig. 3(b). The samples with larger α_{eff} values show smaller signal-to-noise ratios in high-T FMR measurements. The measurements are carried out over a temperature range of $T = 25$–$600\,°\mathrm{C}$. The measurement data are presented in Fig. 5.

Figure 5(a) gives H_{eff} as a function of T, where the H_{eff} data are calculated using Eq. (1) with the experimentally measured H_{FMR} data [see Fig. 4(b)] and a gyromagnetic ratio of $|\gamma| = 2.8$ MHz/Oe. Two main results are evident from the data in Fig. 5(a). First, in all the samples, H_{eff} decreases with an increase in T. This result is most likely associated with the fact that the hard FePt layer has a Curie temperature of around $T_c \approx 425\,°\mathrm{C}$ [18] while the soft FTM layers usually have a much higher T_c. For example, T_c in bulk Co is about $1130\,°\mathrm{C}$ [34]. T_c in Co thin films may be slightly lower than $1130\,°\mathrm{C}$, but should be substantially

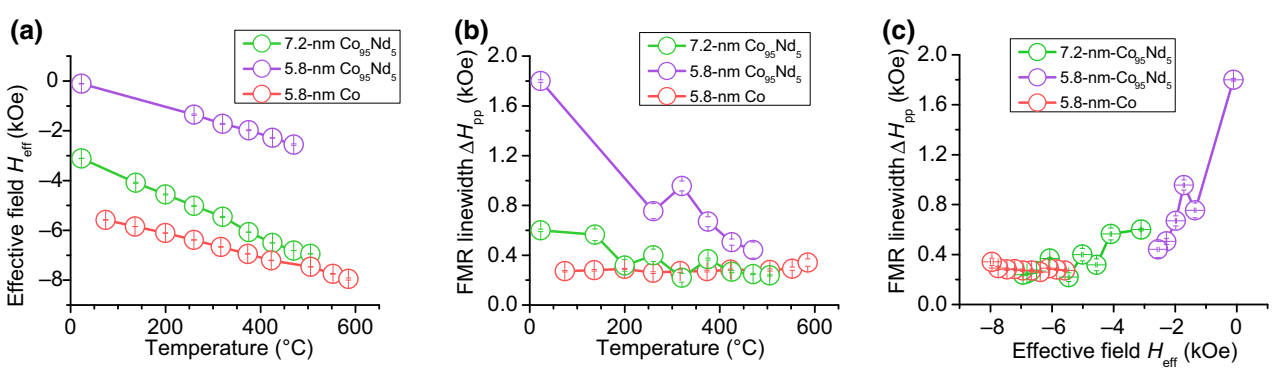

FIG. 5. Data from high-temperature FMR studies. (a) and (b) present the effective internal field (H_{eff}) and the FMR linewidth (ΔH_{pp}), respectively, as a function of temperature for three samples with different soft layers, as indicated. (c) Plots ΔH_{pp} as a function of H_{eff}. The ΔH_{pp} data are from (b), while the H_{eff} data are from (a).

higher than 425 °C [35]. Thanks to this difference in T_c, $4\pi M_s$ in the hard FePt layer drops faster than that in the soft FTM layer when T is increased toward 600 °C. The net effect is that with an increase in T, H_{ex} drops by a larger amount than the $4\pi M_s$ of the FTM layer and H_{eff} decreases accordingly. Note that H_{ex} strongly depends on the magnetic moment in the hard FePt layer. Second, the 5.8-nm $Co_{95}Nd_5$ sample shows larger H_{eff} values than the other two over the entire T range, indicating larger H_{ex} in this sample. This is because the soft FTM layer in this sample is thinner than in the 7.2-nm $Co_{95}Nd_5$ sample and has a smaller $4\pi M_s$ value than in the 5.8-nm Co sample. Thus, this result is generally consistent with the conclusion drawn from the data in Fig. 3(a).

Figure 5(b) presents the ΔH_{pp} vs T data of the three samples. One can see that the T dependence of ΔH_{pp} differs remarkably in the three samples. ΔH_{pp} in the 5.8-nm $Co_{95}Nd_5$ sample shows a rather strong T dependence. ΔH_{pp} decreases by a factor of 5 when T is increased from 23 °C to 467 °C. In contrast, ΔH_{pp} in the 7.2-nm $Co_{95}Nd_5$ sample shows a much weaker T dependence and ΔH_{pp} in the 5.8-nm Co sample is almost constant.

These results can be understood in terms of the T dependence of the two damping components in Eq. (4). Specifically, over the T range considered here, α_0 results mainly from spin-flip magnon-electron scattering. This scattering process requires both momentum and energy conservations, which can be satisfied more easily at high T [28–30]. As a result, α_0 is expected to increase with T. In contrast, α_{sp} is expected to decrease with T because IEC is weaker and H_{ex} is smaller at higher T as suggested by the data presented in Fig. 5(a).

For the 5.8-nm $Co_{95}Nd_5$ sample, H_{eff} is almost zero at room temperature, as shown in Fig. 5(a), indicating $H_{ex} \approx 4\pi M_s$. This means that IEC in this sample is relatively strong and α_{sp} dominates over α_0 at room temperature. With an increase in T, IEC becomes weaker and α_{sp} becomes smaller, giving rise to the large ΔH_{pp} drop shown in Fig. 5(b).

The situation is completely different in the 5.8-nm Co sample. In this sample, H_{eff} is very small, as shown in Fig. 5(a). This indicates that IEC is relatively weak and α_{sp} may be comparable with α_0. With an increase in T, α_{sp} decreases while α_0 increases, resulting in an overall flat response for ΔH_{pp}, as shown in Fig. 5(b). When T is close to or higher than T_c, α_{sp} becomes so small that α_0 starts to become dominant. Since α_0 increases with T as discussed above, ΔH_{pp} shows a slight increase over the T range of 500–600 °C.

In addition, the data in Fig. 5(b) also show that the three samples show comparable ΔH_{pp} values near T_c, although they show very different ΔH_{pp} values near room temperature. This observation supports the above interpretation. In brief, near room temperature, H_{ex} is very different in the three samples, resulting in very different α_{sp} values and very different ΔH_{pp} values. Near T_c, IEC becomes absent in all the samples, resulting in negligible α_{sp} and comparable ΔH_{pp} values.

One can clearly see from the above discussions that IEC plays critical roles in the T dependence of the FMR linewidth. To further illustrate this, ΔH_{pp} is plotted against H_{eff} in Fig. 5(c) in a way similar to the plot in Fig. 3(c). Note that both the changes of H_{ex} and $4\pi M_s$ with T contribute to the variation of H_{eff}, but H_{ex} plays a bigger role due to the difference in T_c between the FePt and FTM layers, as discussed above. The plot surprisingly shows the same trend as the one in Fig. 3(c), even though the data here are measured at very different temperatures while all the data in Fig. 3(c) are measured at the same temperature, namely, room temperature. This consistency evidently confirms the above-discussed H_{ex}-damping correlation.

One can also see from the data in Fig. 5(c) that even though the overall trend is the increase of ΔH_{pp} with H_{eff}, the slope varies notably with H_{eff}. It is large in the relatively high H_{eff} region and almost zero in the very low H_{eff} region. This is consistent with the above interpretation of the ΔH_{pp} data presented in Fig. 5(b).

VII. CONCLUSIONS AND OUTLOOK

In summary, broadband FMR and high-temperature (T) FMR measurements are carried out to study IEC in a magnetic hard-soft bilayered system where the hard layer is a $L1_0$-ordered FePt thin film and the soft layer is a FTM thin film. The data indicate that the IEC-produced exchange field (H_{ex}) on the soft layer strongly depends on the choice of material of the soft layer as well as the soft layer thickness. The thinner the soft layer is and the smaller $4\pi M_s$ the soft layer has, the larger the field H_{ex} is. With an increase in T, H_{ex} drops by a larger amount than the $4\pi M_s$ of the soft layer, resulting in an effective internal field that decreases with T. The IEC strongly affects the FMR linewidth and damping of the soft layer. The general trend is that both the FMR linewidth (ΔH) and the effective Gilbert damping constant (α_{eff}) increase with H_{ex}, but there are also several subtle effects associated with H_{ex}. In the $H_{ex} > 4\pi M_s$ regime, α_{eff} is insensitive to the choice of material of the soft layer. In the $H_{ex} < 4\pi M_s$ regime, however, α_{eff} strongly depends on the choice of material. With an increase in T, ΔH decreases substantially in samples where H_{ex} is relatively large, but remains constant or even increases slightly in samples where H_{ex} is very small.

Note that the wide tuning of IEC, H_{ex}, and α_{eff} demonstrated in this work is realized through changes in the soft layer thickness and the material of the soft layer, but they can also be tuned through doping different impurities into the soft layer, controlling interface quality, or varying the properties of the hard layer. Future experimental studies on such tunability are of great interest.

ACKNOWLEDGMENTS

This work was mainly supported by Western Digital. In addition, the FMR measurements were also supported by the U.S. National Science Foundation under Grant No. EFMA-1641989 and the FMR data analysis was supported by the U.S. Department of Energy, Office of Science, Basic Energy Sciences under Grant No. DE-SC0018994.

APPENDIX

Figure 6 gives the magnetic hysteresis loops of hard-soft FePt/FTM bilayered samples measured by polar MOKE techniques. The thickness values of the soft FTM layers are indicated in the figure. The hysteresis loops all look clean and smooth and show almost 100% remanence at zero fields. No two-stage switching is observed. These results show that the hard FePt layers have perpendicular anisotropy and the soft FTM layers are tightly coupled to the FePt layers.

Figure 7 presents the coercivity values of the hard-soft FePt/FTM bilayered samples, which are determined according to the hysteresis loops given in Fig. 6. The data show that for a given soft material, the coercivity of the bilayered sample decreases with an increase in the thickness of the soft layer; for a given soft layer thickness, the coercivity varies with the choice of the soft material. These results are consistent with the general expectation on the roles of the soft layer in the switching of the hard layer in a hard-soft bilayered system.

The subsection below shows how to extract the FMR field and linewidth parameters in magnetic thin films with relatively large damping from broadband FMR measurement data. It is known that the power absorbed during an FMR measurement is given by

$$P = -\frac{1}{2}\omega|h_0|^2\mathrm{Im}(\chi), \tag{A1}$$

where ω is the angular frequency of the external microwave, h_0 is the amplitude of the microwave field, and χ is the magnetic susceptibility of the film. $-\mathrm{Im}(\chi)$ can be derived from the Gilbert equation in the usual manner

$$-\mathrm{Im}(\chi) = \frac{\frac{\omega_M}{4\pi}[\alpha\omega\omega_y^2 + \alpha\omega^3(\alpha^2+1)]}{\{[(\omega_x\omega_y)^2 - \omega^2(\alpha^2+1)]^2 + \alpha^2\omega^2(\omega_x+\omega_y)^2\}}, \tag{A2}$$

where α is the Gilbert damping constant. There have been no assumptions based on the value of α, whereas most previous works have utilized $\alpha^2 \ll 1$. ω_M in Eq. (A2) is defined as

$$\omega_M = |\gamma|4\,\pi M_s, \tag{A3}$$

where $|\gamma|$ is the absolute gyromagnetic ratio and is usually close to $2\pi \times 2.8$ MHz/Oe. Because only the out-of-plane configuration is of interest here, one can write

$$\omega_x = \omega_y = |\gamma|(H_0 + H_{\mathrm{eff}}), \tag{A4}$$

where H_{eff} is the effective internal field given by

$$H_{\mathrm{eff}} = H_{\mathrm{ex}} - 4\pi M_s. \tag{A5}$$

H_0 in Eq. (A4) is the external static magnetic field applied perpendicular to the film plane. Following the previous methods for deriving an equation for the FMR linewidth,

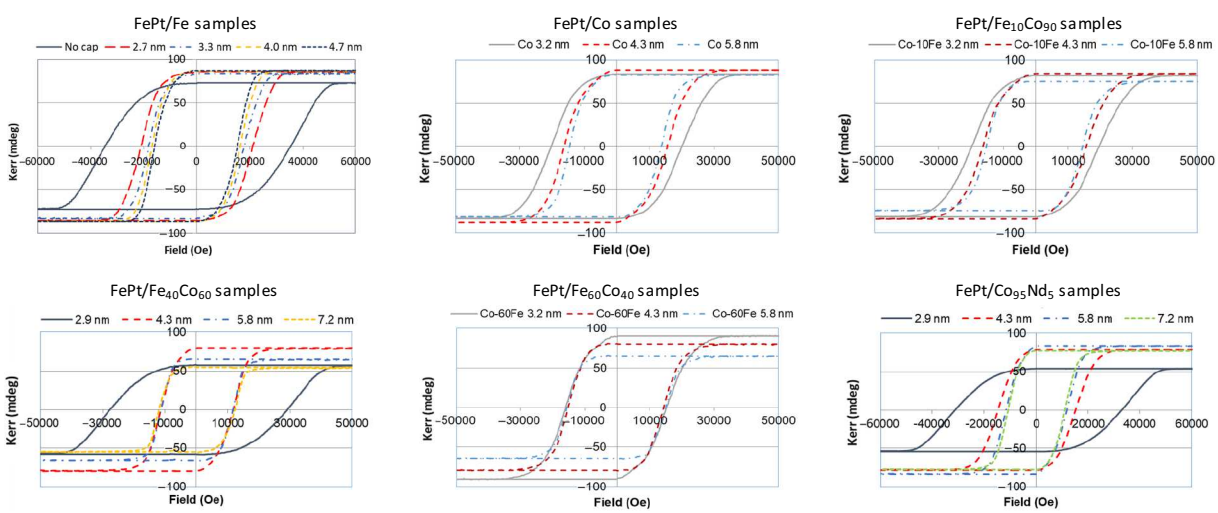

FIG. 6. Magnetic hysteresis loops of hard-soft bilayered samples measured by polar MOKE techniques. The thicknesses of the soft layers are given in the figure.

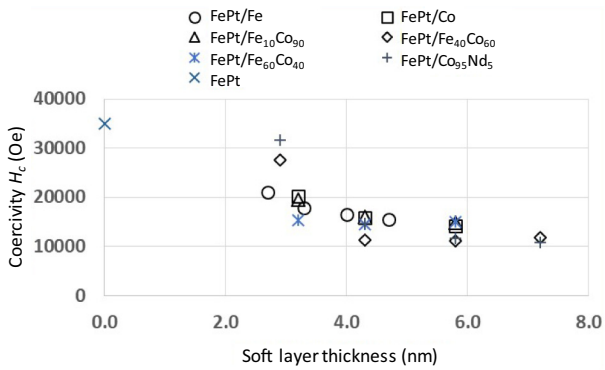

FIG. 7. Coercivities of the hard-soft bilayered samples obtained from the hysteresis loops presented in Fig. 6.

the first step is to find the maximum power and then divide it by 2 to find the half maximum power. To do so, one evaluates

$$\left.\frac{\partial P}{\partial H_0}\right|_{\omega} = 0. \tag{A6}$$

Since the applied field is the quantity that is changing during the measurements, the frequency is considered to be fixed. The value of H_0 that satisfies Eq. (A2) by making P a maximum is

$$H_{P\max} = \frac{\omega}{|\gamma|}\sqrt{2\sqrt{\alpha^2+1}-\alpha^2-1} - H_{\text{eff}}. \tag{A7}$$

In the limit of $\alpha^2 \ll 1$, the resonance condition for zero damping is recovered. The second step is to find H_0 at both of the two half-maximum power values as well. To do this, one writes

$$\frac{1}{2}P(H_{P\max}) = P(H_0). \tag{A8}$$

With Eq. (A1), Eq. (A8) can be rewritten as

$$\frac{1}{2}\text{Im}[\chi(H_{P\max})] = \text{Im}[\chi(H_0)]. \tag{A9}$$

Equation (A9) gives two solutions for H_0. One is for the half maximum on the left side of the peak, while the other is for the half maximum on the right side of the peak. The difference in these two will give the FMR linewidth ΔH. Note that ΔH is associated with the peak-to-peak linewidth by

$$\sqrt{3}\Delta H_{\text{pp}} = \Delta H. \tag{A10}$$

The above procedure gives rise to a linewidth as

$$\Delta H = G(\alpha)\frac{2(2\pi f)}{|\gamma|}, \tag{A11}$$

where $G(\alpha)$ is given by

$$G(\alpha) = x - y, \tag{A12}$$

$$x = \sqrt{\frac{\left(\alpha^2-\sqrt{\alpha^2+1}+1\right)\alpha + \alpha\sqrt{\left(\alpha^2-\sqrt{\alpha^2+1}+1\right)^2 - \frac{\alpha^2}{4}(\alpha^2+1) + \sqrt{\alpha^2+1}\left(\alpha^2-\sqrt{\alpha^2+1}+1\right)} + \frac{\alpha}{4}\sqrt{\alpha^2+1} - \frac{\alpha^3}{4}\sqrt{\alpha^2+1}}{\alpha\sqrt{\alpha^2+1}}},$$

$$y = \sqrt{\frac{\left(\alpha^2-\sqrt{\alpha^2+1}+1\right)\alpha - \alpha\sqrt{\left(\alpha^2-\sqrt{\alpha^2+1}+1\right)^2 - \frac{\alpha^2}{4}(\alpha^2+1) + \sqrt{\alpha^2+1}\left(\alpha^2-\sqrt{\alpha^2+1}+1\right)} + \frac{\alpha}{4}\sqrt{\alpha^2+1} - \frac{\alpha^3}{4}\sqrt{\alpha^2+1}}{\alpha\sqrt{\alpha^2+1}}}.$$

The equation used to fit the real and imaginary parts of the experimentally measured complex transmission coefficient S_{21} can be written as

$$S_{21} = S_{21}^0 + DH_0 + \frac{\chi}{\chi_0}, \tag{A13}$$

where the first term on the right side describes the electronic background, the second denotes the linear electronic drift during the sweeping of the field, and χ_0 is the usual fitting parameter that has experimental parameters built in. Each term in Eq. (A13) has

a real part and an imaginary part associated with it, namely,

$$S_{21}^0 = \mathrm{Re}(S_{21}^0) + i\mathrm{Im}(S_{21}^0), \tag{A14}$$

$$DH_0 = \mathrm{Re}(DH_0) + i\mathrm{Im}(DH_0), \tag{A15}$$

$$\frac{\chi}{\chi_0} = \mathrm{Re}\left(\frac{\chi}{\chi_0}\right) + i\mathrm{Im}\left(\frac{\chi}{\chi_0}\right), \tag{A16}$$

where $\chi = \chi_R + i\chi_I$ and $\chi_0 = \chi_{0R} + i\chi_{0I}$ so that

$$\frac{\chi}{\chi_0} = \frac{1}{\chi_{0R}^2 + \chi_{0I}^2}[(\chi_{0R}\chi_R + \chi_{0I}\chi_I) - i(\chi_{0R}\chi_I + \chi_{0I}\chi_R)]. \tag{A17}$$

The imaginary part χ_I was given earlier for finding the linewidth. The real part is

$$\chi_R = \frac{\frac{\omega_M}{4\pi}[\omega_y^3 + \omega_y\omega^2(\alpha^2 - 1)]}{\{[\omega_y^2 - \omega^2(\alpha^2 + 1)]^2 + 4\alpha^2\omega^2\omega_y^2\}}. \tag{A18}$$

The parameters S_{21}^0, D, and χ_0 have physical information about the VNA FMR setup and the sample built in and must be determined through the fitting of the S_{21} profiles.

The Gilbert damping constant α can be obtained by fitting the S_{21} profiles with Eq. (A13). By repeating this process for the S_{21} data measured at different frequencies, one obtains the damping constants at different frequencies. The results usually show that the damping constant decreases with an increase in the frequency, but the Gilbert damping constant is known to be frequency independent. This apparent change is actually due to spatial film inhomogeneity caused FMR linewidth broadening. To reconcile this problem, Eq. (A11) is used to calculate a FMR linewidth from the damping constant at each frequency. The real damping constant can then be obtained by fitting the linewidth vs frequency data using

$$\Delta H = G(\alpha)\frac{2(2\pi f)}{|\gamma|} + \Delta H_{\mathrm{ILB}}, \tag{A19}$$

where ΔH_{ILB} denotes the contribution from the film inhomogeneity line broadening and is frequency independent. This fitting yields the true Gilbert damping constant, which does not change with frequency. Thus, the procedure for the determination of the Gilbert damping constant α in thin films with relatively large α includes the following major steps:

(1) Measure S_{21} as a function of the field at a fixed frequency.

(2) Fit the S_{21} profiles with Eq. (A13) to determine the α value.

(3) Use the α value and Eq. (A11) to calculate the FMR linewidth ΔH.

(4) Repeat steps (1)–(3) for different frequencies.

(5) Plot the FMR linewidth ΔH as a function of the frequency and then fit the data with Eq. (A19) to obtain the true α.

[1] D. Suess, T. Schrefl, S. Fahler, M. Kirschner, G. Hrkac, F. Dorfbauer, and J. Fidler, Exchange spring media for perpendicular recording, Appl. Phys. Lett. **87**, 012504 (2005).

[2] A. Berger, N. Supper, Y. Ikeda, B. Lengsfield, A. Moser, and E. Fullerton, Improved media performance in optically coupled exchange spring layer media, Appl. Phys. Lett. **93**, 122502 (2008).

[3] G. Choe, M. Zheng, B. Acharya, E. Abarra, and J. Zhou, Perpendicular recording CoPtCrO composite media with performance enhancement capping layer, IEEE Trans. Magn. **41**, 3172 (2005).

[4] H. Jung, E. Velu, S. Malhotra, G. Bertero, and U. Kwon, Comparison of media properties between hard/soft stacked composite and capping layer perpendicular recording media, J. Magn. Magn. Mater. **320**, 3151 (2008).

[5] Y. Tserkovnyak, A. Brataas, and G. E. W. Bauer, Enhanced Gilbert Damping in Thin Ferromagnetic Films, Phys. Rev. Lett. **88**, 117601 (2002).

[6] B. Heinrich, Y. Tserkovnyak, G. Woltersdorf, A. Brataas, R. Urban, and G. E. W. Bauer, Dynamic Exchange Coupling in Magnetic Bilayers, Phys. Rev. Lett. **90**, 187601 (2003).

[7] E. Simanek and B. Heinrich, Gilbert damping in magnetic multilayers, Phys. Rev. B **67**, 144418 (2003).

[8] W. Zhang, M. B. Jungfleisch, W. Jiang, J. Sklenar, F. Y. Fradin, J. E. Pearson, J. B. Ketterson, and A. Hoffmann, Spin pumping and inverse Rashba-Edelstein effect in NiFe/Ag/Bi and NiFe/Ag/Sb, J. Appl. Phys. **117**, 172610 (2015).

[9] J. Tsai, H. Tzeng, and G. Lin, Magnetization reversal process in Fe/FePt films, Appl. Phys. Lett. **96**, 032505 (2010).

[10] H. Guo, J. Liao, Z. Zhang, Q. Jin, W. Rui, J. Du, H. Wang, and J. Wang, $L1_0 - FePt$ based exchange coupled composite films with soft $[Co/Ni]_N$ multilayers, Appl. Phys. Lett. **111**, 103916 (2012).

[11] Z. Liu, Y. Jiao, and R. H. Victora, Composite media for high density heat assisted magnetic recording, Appl. Phys. Lett. **108**, 232402 (2016).

[12] N. Naterkar, Z. Liu, S. Hernandez, and R. H. Victora, SNR improvement of variation of recording and media parameters for a HAMR exchange coupled composite media, AIP Adv. **8**, 056513 (2018).

[13] D. Weller, G. Parker, O. Mosendz, E. Champion, B. Stipe, X. Wang, T. Klemmer, G. Ju, and A. Ajan, A HAMR media

technology roadmap to an areal density of 4 Tb/in^2, IEEE Trans. Magn. **50**, 3100108 (2014).

[14] M. Schoen, D. Thonig, M. Schneider, T. Silva, H. Nembach, O. Eriksson, O. Karis, and J. Shaw, Ultra-low damping of a metallic ferromagnet, Nat. Phys. **12**, 839 (2016).

[15] Y. Zhang, A. Kalitsov, J. Ciston, O. Mryasov, B. Ozdol, J. Zhu, S. Jain, B. Zhang, B. Livshitz, A. Chernyshov, A. Ajan, P. Dorsey, G. Bertero, R. Acharya, A. Greene, and S. Myers, Microstructure and magnetic properties of ultrathin FePt granular films, AIP Adv. **8**, 125018 (2018).

[16] L. Lu, M. Wu, M. Mallary, G. Bertero, K. Srinivasan, R. Archarya, H. Schultheiß, and A. Hoffmann, Observation of microwave-assisted magnetization reversal in perpendicular recording media, Appl. Phys. Lett. **103**, 042413 (2013).

[17] D. Richardson, K. Srinivasan, S. Katz, and M. Wu, Quantification of intergranular exchange coupling in CoPtCr-based perpendicular recording media via ferromagnetic resonance measurements, Appl. Phys. Lett. **111**, 183506 (2017).

[18] D. Richardson, S. Katz, J. Wang, Y. K. Takahashi, K. Srinivasan, A. Kalitsov, K. Hono, A. Ajan, and M. Wu, Near-T_c Ferromagnetic Resonance and Damping in FePt-Based Heat-Assisted Magnetic Recording Media, Phys. Rev. Appl. **10**, 054046 (2018).

[19] J. Becker, O. Mosendz, D. Weller, A. Kirilyuk, J. C. Maan, P. C. M. Christianen, Th. Rasing, and A. Kimel, Laser induced spin precession in highly anisotropic granular $L1_0$ FePt, Appl. Phys. Lett. **104**, 152412 (2014).

[20] Y. Ding, T. J. Klemmer, and T. M. Crawford, A coplanar waveguide permeameter for studying high-frequency properties of soft magnetic materials, J. Appl. Phys. **96**, 2969 (2004).

[21] H. T. Nembach, T. J. Silva, J. M. Shaw, M. L. Schneider, M. J. Carey, S. Maat, and J. R. Childress, Perpendicular ferromagnetic resonance measurements of damping and Lande g-factor in sputtered $(Co_2Mn)_{1-x}Ge_x$ thin films, Phys. Rev. B **84**, 054424 (2011).

[22] The expectation of Hex∝(Ms·d)-1 in hard-soft bilayered systems had been shown in unpublished calculations carried out by Alan Kalitsov and Oleg Mryasov.

[23] M. Sparks, *Ferromagnetic-Relaxation Theory* (McGraw-Hill, New York, 1964).

[24] R. D. McMichael and P. Krivosik, Classical model of extrinsic ferromagnetic resonance linewidth in ultrathin films, IEEE Trans. Magn. **40**, 2 (2004).

[25] P. Landeros, Rodrigo E. Arias, and D. L. Mills, Two magnon scattering in ultrathin ferromagnets: The case where the magnetization is out of plane, Phys. Rev. B **77**, 214405 (2008).

[26] N. Mo, J. Hohlfeld, M. ul Islam, C. S. Brown, E. Girt, P. Krivosik, W. Tong, A. Rebei, and C. E. Patton, Origins of damping in perpendicular media: Three component ferromagnetic resonance linewidth in Co − Cr − Pt alloy films, Appl. Phys. Lett. **92**, 022506 (2008).

[27] P. Krivosik, S. S. Kalarickal, N. Mo, S. Wu, and C. E. Patton, Ferromagnetic resonance and damping in granular Co − Cr films with perpendicular anisotropy, Appl. Phys. Lett. **95**, 052509 (2009).

[28] J. Kunes and V. Kambersky, First-principles investigation of the damping of fast magnetization precession in ferromagnetic 3d metals, Phys. Rev. B **65**, 212411 (2002).

[29] V. Kambersky, Spin-orbit Gilbert damping in common magnetic metals, Phys. Rev. B **76**, 134416 (2007).

[30] K. Gilmore, Y. U. Idzerda, and M. D. Stiles, Identification of the Dominant Precession-Damping Mechanism in Fe, Co, and Ni by First-Principles Calculations, Phys. Rev. Lett. **99**, 027204 (2007).

[31] T. Qu and R. H. Victora, Effect of substitutional defects on Kambersky damping in $L1_0$ magnetic materials, Appl. Phys. Lett. **106**, 072404 (2015).

[32] M. Oogane, T. Wakitani, S. Yakata, R. Yilgin, Y. Ando, A. Sakuma, and T. Miyazaki, Magnetic damping in ferromagnetic thin films, Jpn. J. Appl. Phys. **45**, 3889 (2006).

[33] S. S. Kalarickal, P. Krivosik, J. Das, K. S. Kim, and C. E. Patton, Microwave damping in polycrystalline Fe − Ti − N films: Physical mechanisms and correlations with composition and structure, Phys. Rev. B **77**, 054427 (2008).

[34] B. Cullity and C. Graham, *Introduction to Magnetic Materials* (Wiley, Hoboken, NJ, 2009).

[35] P. Bruno, Theory of the Curie temperature of cobalt-based ferromagnetic ultrathin films and multilayers, J. Magn. Soc. Jpn. **15**, 15 (1991).